Dalton Transactions

ROYAL SOCIETY OF CHEMISTRY

PAPER

View Article Online
View Journal

Check for updates

Cite this: DOI: 10.1039/d0dt02278k

Micro–nano NiO-MnCo$_2$O$_4$ heterostructure with optimal interfacial electronic environment for high performance and enhanced lithium storage kinetics†

Wei Dang,[a] Xincun Tang, *[a] Wei Wang,[b] Yun Yang,[c] Xing Li,[a] Liuchun Huang[a] and Yi Zhang *[a]

Received 28th June 2020,
Accepted 17th July 2020

DOI: 10.1039/d0dt02278k

rsc.li/dalton

This manuscript provides an *in situ* synthesis method for the self-assembly of a heterostructured NiO-MnCo$_2$O$_4$ micro–nano composite with a poriferous shell. The special shell structure effectively alleviated the volume variation and subsequently enhanced the diffusivity of ions in the cycling process for cyclic stability. The inner spaces among the stacked nanoparticles are conducive to electrolyte infiltration and the transfer of ion/electrons with low concentration polarization. Consequently, the optimized NiO-MnCo$_2$O$_4$ exhibited excellent cycle stability (718.8 mA h g^{-1} after 1000 cycles at 2 A g^{-1}) and highly recoverable rate performance. On gaining insight into the heterointerface structure, it was indicated that the optimal interfacial electronic environment in the presence of the nickel content plays a key role in creating lattice defects and active sites to increase the ion diffusion rate, electron conductivity and unlock extra pseudocapacitance for ion storage. The excellent capabilities from the optimal heterointerface environment will promote the development of high-energy applications of LIBs.

1. Introduction

LIBs have been widely applied in products ranging from portable electronic devices to the double-source EV because of their long lifetime, high energy density, *etc.*[1–3] However, the conventional electrode materials, such as graphite-based anodes with theoretical capacity only reaching 372 mA h g^{-1}, hardly meet the high demand for hybrid electric vehicles and some electronics.[4] During the charging–discharging process at high rates, safety problems might occur.[5,6] As such, the high-performance electrode materials (cycle stability, high energy density and rate stability) should be explored to meet the rapidly increasing energy demand.

Many kinds of promising alternative anode materials, such as TMOs, have been developed owing to their low cost, safety and high capacity.[7–11] Unfortunately, single-phase TMOs are also limited by their poor cycle performance because of their intrinsic weakness in electrical/ionic conductivity, as well as the large variation in the volume.[12,13] Many innovative achievements have been discovered in complex TMOs, such as Co$_3$O$_4$-MnCo$_2$O$_4$, Ni-MnCo$_2$O$_4$, NiO-Co$_3$O$_4$, CoO-NiO-C and Fe$_2$O$_3$-Co$_3$O$_4$.[14–18] In particular, the MnCo$_2$O$_4$-based polymetallic oxides that have high capacity, environmental friendliness and low price have been the focus for electrode materials for LIBs.[19] The disadvantages of MnCo$_2$O$_4$-based electrode materials include their relatively low operating voltage and low specific capacitance. As an electrode material, further improvement of the inferior structural stability of MnCo$_2$O$_4$ during the electrochemical cycle is a major challenge; this improvement should lead to the enhancement of its cycling stability and energy storage capability for high power density sources. Therefore, we constructed a hybrid heterostructure, NiO-MnCo$_2$O$_4$ micro–nano crystals, *via* self-assembly and calcination. This design and synthesis route involves two processes: (i) the construction of the poriferous core–shell architecture with the oxides/oxides to realize the structural stability as well enhance the diffusivity of ions.[14–17] (ii) The formed heterogeneous structures (coupling nanocrystals with different bandgaps) can effectively provide the advantages of transport paths for ions and electrons.[20–25]

The synthesis details of NiO-MnCo$_2$O$_4$ are illustrated in Fig. 1a. The uniform Ni–Mn–Co oxalate precursor was prepared *via* a coprecipitation process that finally resulted in the hybrid

---

[a] *College of Chemistry and Chemical Engineering, Central South University, Changsha 410083, P. R. China. E-mail: txincun@163.com, yzhangcsu@csu.edu.cn*
[b] *Key Laboratory of Hunan Province for Advanced Carbon-based Functional Materials, School of Chemistry and Chemical Engineering, Hunan Institute of Science and Technology, Yueyang, 414006, P. R. China*
[c] *Key Laboratory of Ministry-of-Education for the Synthesis and Application of Organic Functional Molecules, College of Chemistry and Chemical Engineering, Hubei University, Wuhan 430062, P. R. China*

† Electronic supplementary information (ESI) available. See DOI: 10.1039/d0dt02278k

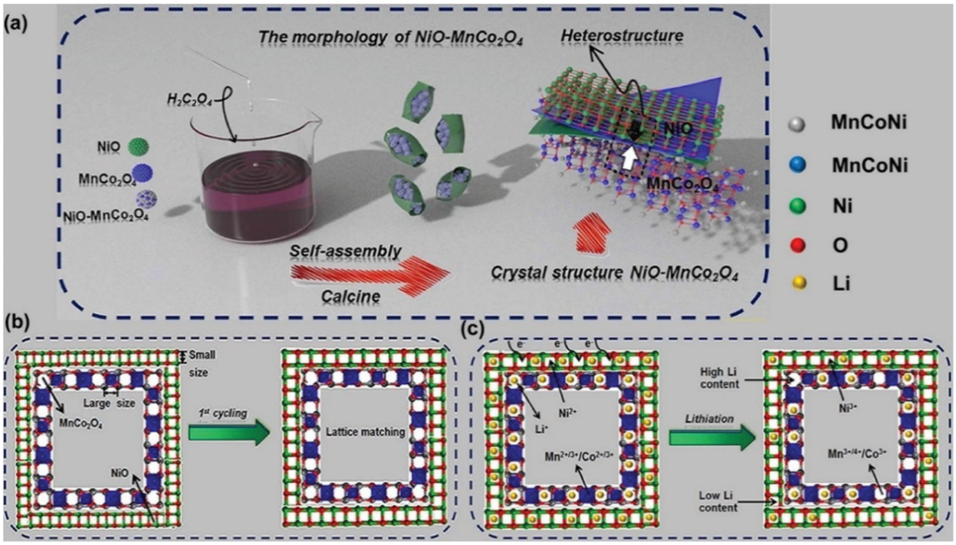

Fig. 1 Schematic illustration showing (a) the formation processes of the prepared S-N-MC, (b) the lattice matching process about the shell–core during the first cycle; (c) the extraction process of Li^+ ions.

heterostructure NiO-$MnCo_2O_4$ after calcination treatment. The procreant two-phase boundaries of NiO-$MnCo_2O_4$ have many active sites and extrinsic defects for fast electron/ion transportation and the lattice matching process between the two phases (NiO shell and $MnCo_2O_4$ core) would appear in the first cycle (Fig. 1b) and subsequently remain stable with the extraction process of Li^+ ions and electrons (Fig. 1c). In brief, the porous shell and internal porous structure serve as an adequate storage container and boost the diffusion of lithium but also mitigates the volumetric variation during the long cycling. On the other hand, the NiO-$MnCo_2O_4$ heterostructure, with lattice defects and oxygen vacancies, effectively contributes to the accelerated electron transfer for compound conversion reactions. According to the molecular dynamics theory, the pseudocapacitive behavior of the hybrid agrees with the adsorption of lithium ions from defects in the lattice, leading to the large exposure of active sites around the heterojunction interface. GITT technology confirmed that the complex TOMs with faster redox/conversion reacting rates presented a higher lithium diffusion resulting from the complex crystal structure with lattice aberrance and the interaction among elements. The electron density difference further illustrates the optimal interfacial electronic environment and the ion/electron transport mechanism in detail at the heterojunction interface. Hence, our work should inspire further host design for fabricating various hybrid anode materials with optimized heterogeneous interfaces, accelerating the development of high-energy-density for LIBs.

2. Experimental section

2.1 Synthesis of the S-N-MC heterostructured microcomposite

The MC_2O_4 (M = Ni, Mn, Co) oxalate precursor was synthesized *via* a facile self-assembly process using oxalate and $M(Ac)_2·4H_2O$ as the precipitant and metal source, respectively. The oxalate (2.0 g) and $Mn(Ac)_2·4H_2O$ (0.7892 g), $Co(Ac)_2·4H_2O$ (1.026 g), and $Ni(Ac)_2·4H_2O$ (0.7764 g) were respectively dissolved in deionized water (50 ml), marked as solution A and B. After continuous magnetic stirring for 30 min, solution A was slowly added to solution B and ultrasonicated for 20 min. The mixed turbid solution including the metal cation and oxalate was in a water bath at 80 °C for 4 h. The precursor was then obtained *via* extraction filtration. The precursor was dried at 60 °C for 12 hours hermetically and after high-temperature calcination in the air, it was marked as S-N-MC. NiO and $MnCo_2O_4$ (named S-N, S-MC) were also obtained by the above flow path. Nickel element was doped in different amounts to determine the effect on the electrochemical performance of the single electrode; therefore, the nickel element content was reduced and then increased to synthesize samples S-N1-MC, S-N2-MC for comparison.

2.2 Characterization of the samples

Field emission SEM images, EDS spectra and atomic mapping images were acquired using a JSM-IT300LA emission scanning electron microscope. Internal characterization and lattice analysis of the synthetic samples were conducted *via* transmission electron microscopy (TEM and HTEM, JEM-2100F). XRD characterization of the prepared materials was performed using a Bruker D8 diffractometer. TG (PerkinElmer Diamond TG/DTA) was conducted in an air atmosphere with a ramp rate of 4 °C min^{-1}. XRD diffraction patterns were fitted to pinpoint the changes in lattice parameters using the GSAS/EXPGUI software. Specific surface and aperture analyzers (BET, Micromeritics ASAP2020) were used to further analyze the phase characteristics. ICP-OES (Optima 5300DV) and FT-IR (Nicolet6700) was used to determine the elementary compositions and the vibrations of the valence bond. The valence states of the component were determined by X-ray photoelectron spectroscopy (XPS, ESCALAB250).

2.3 Electrochemical measurements

The prepared half-cell, including the active material and Li as the cathode/anode, was used to confirm the electrochemical performances. For the cathode, the active material (*e.g.* S-N-MC), carbon black (Super P), and polyvinylidene fluoride (PVDF) were evenly mixed in an 8 : 1 : 1 (wt%) ratio in *N*-pyrrolidinone (NMP) and the black uniform slurry was evenly painted on Cu foil *via* a doctor blade. After vacuum drying overnight, the cathode wafer with a diameter of about 11 mm was prepared by punching and the active mass loading of the active material is about 0.69 mg cm^{-2}. The organic electrolyte was made up of 1 M $LiPF_6$ with EC and DEC (1 : 1 : 1 by volume). CR2016 coin-type half-cells were sealed with a separator (Celgard2400) in the argon glove box. GCD tests and GITT were carried out at room temperature on the Neware test system; the relaxation period was set as 8 min at 500 mA g^{-1} at 0.01–3.0 V (*vs.* Li/Li^+). The CV and EIS tests both used the ZIVE-SP1 electrochemical workstation.

3. Results and discussion

3.1 Structure and morphology characterization

Fig. 2 shows typical SEM and low TEM images of the as-obtained S-N, S-MC and S-N-MC. The S-N tight microspheres have a rough surface with a diameter of 6.92 μm and a large number of micron spheres crosslinked with each other from some group-like structures, similar to grape clusters in Fig. 2a and b. Compared with the compact structure of nickel oxide, S-MC has smaller particles (≈300 nm) and presents as a club-like agglomeration of nanoparticles with lots of voids as shown in Fig. 2c and d. Fig. 2e and f show the as-obtained S-N-MC, which present a micro–nano structure with a dense shell and the interior of the shell is constructed by the staggered growth of irregular nanoparticles. The three as-prepared samples presented the uniform agglomeration of particles as seen from the inset of Fig. 2a and c–e, while the elements of S-N-MC were evenly distributed according to the element mapping images in Fig. 2g. EDS spectroscopy analysis (Fig. S1a, ESI†) further indicated the distribution of metallic elements, which agrees with the ICP-OES results (see Table S2†).

The formation mechanism of the sample could be explained as follows: the preference for Mn^{2+} and Co^{2+} coordination with $C_2O_4^{2-}$ reunites chains, which can be interlinked to form a nanoparticle. Through hydrogen bonding, these primary particles are stacked upon one another and further bundled into the rod-like structure after the second sintering. However, as the most influential factor on the final morphology of the nanomaterials, the different interfacial tensions usually affect the growth of different crystal faces.[26] Therefore, after adding the nickel to affect the overall metal concen-

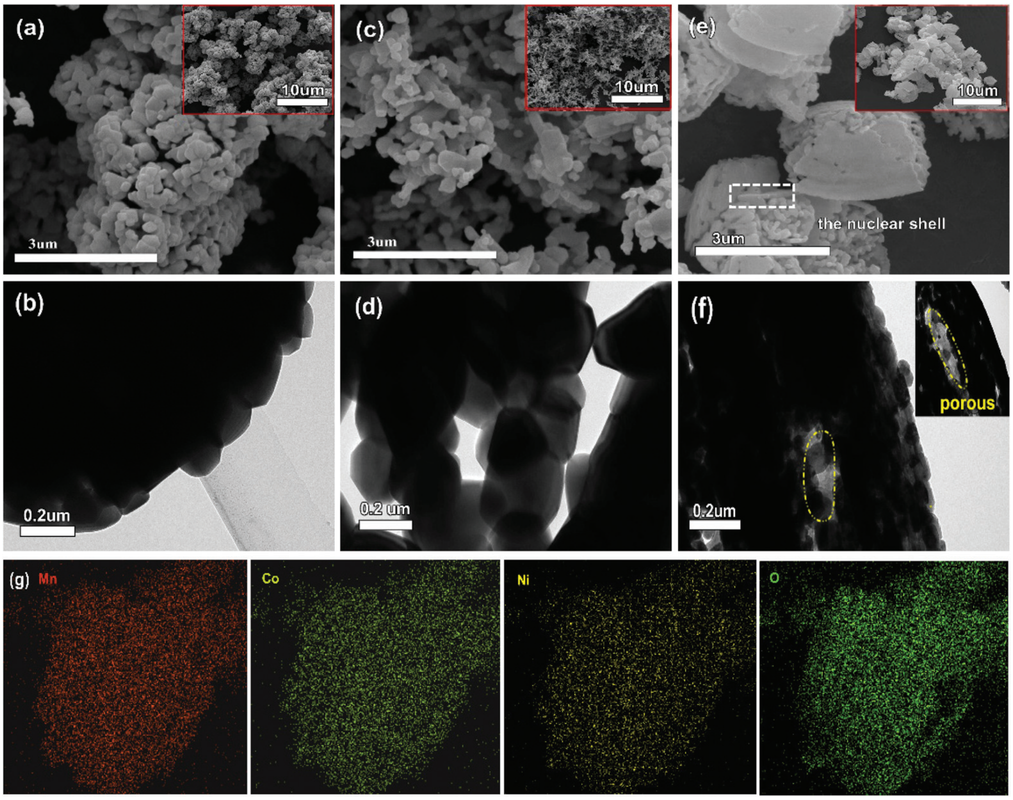

Fig. 2 SEM and typical TEM images of (a and b) S-N, (c and d) S-MC and (e and f) S-N-MC. (g) Elemental mapping images of S-N-MC.

tration, micro–nano structures with compact shell interfaces were formed due to the possible interfacial tension.

Fig. 3b shows the X-ray diffraction (XRD) results for the S-N (in purple), S-MC (in olive) and S-N-MC (in orange); the three samples can be assigned to NiO (JCPDS no. 65-2901, space group *Fd*3*m*), and the cubic phase of the $MnCo_2O_4$ spinel structure (JCPDS no. 23-1237, space group *Fd*3*m*). The Mn/Co elements in the binary metal oxide $MnCo_2O_4$ were homogeneously mixed in the bivalent and trivalent states, in which Mn(III)/Co(III) occupy the octahedral sites and Mn(II)/Co(II) are distributed over the interstices of the stacked tetrahedra. The crystal structures of the S-N, S-MC are shown in Fig. 3a. The hybrid S-N-MC composed of two cubic phases is similar to that of $MnCo_2O_4$ (see the following Fig. 3h for details), while bivalent cobalt and manganese atoms in the lattice of $MnCo_2O_4$ were replaced by a nickel atom. Since the ionic radius of Ni^{2+} (69 pm) is larger than that of Mn^{2+} (67 pm) and Co^{2+} (65 pm), the lattice parameters of S-N-MC should be larger than those of S-MC. Compared with the S-MC, the peaks located at smaller angles relate to the S-N-MC by the Bragg equation. Additionally, there are no redundant peaks, indicating the high purity of all three samples. Compared with the diffraction intensities of the S-N and S-MC, S-N-MC showed the highest value, as seen from Table S1.† Therefore, S-N-MC has good crystallinity, providing evidence for the higher electrochemical performance. Besides, the high crystallinity of the sample is closely connected to the calcination procedure shown by the thermogravimetric (TG) analysis (seen from Fig. 3c). The Ni : Co : Mn atomic ratio was about 0.647 : 0.389 : 0.472 by the further ICP-OES test (Table S2, ESI†), which is in agreement with the EDS results (in Fig. S1a†).

The corresponding HRTEM micrographs of S-N, S-MC and S-N-MC are presented in Fig. 3d–f. As depicted in Fig. 3d, based on the standard plane value of hexagonal S-N, the obtained 0.24 nm interplanar spacing is similar to the (020) plane (in Fig. 3b), well-matched with the XRD analysis. As seen from Fig. 3e, the *d*-spacing of 0.47 nm with the matching crystal planes (111) of S-MC is wider than that of pure S-N, consistent with the electrochemical properties resulting from the broader lithium-ion transport path. Nevertheless, from Fig. 3f, S-N-MC shows a clear lattice interface and lattice fringes of the heterostructure with a *d*-spacing of 0.47 nm and 0.24 nm, consistent with the (111) crystal planes of $MnCo_2O_4$ and NiO. Due

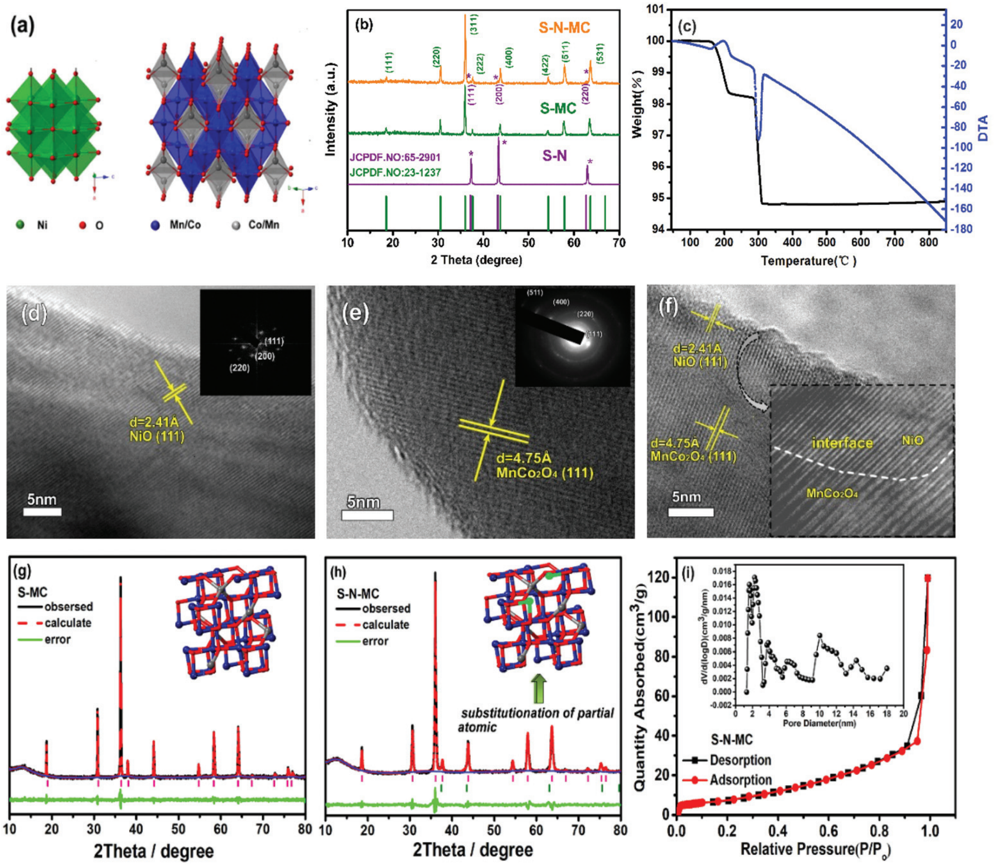

Fig. 3 (a) Crystal structures and lattice parameters of the component S-N and S-MC. (b and l) XRD patterns of the prepared samples. (c) TGA curves of the precursor under an air atmosphere. (d–f and j, k) HRTEM images of S-N, S-MC and S-N-MC, S-N1-MC, S-N2-MC, respectively. (g and h) Rietveld refinement plots of the XRD patterns and unit cells of S-MC and S-N-MC. (i) N_2 adsorption/desorption isotherms and the corresponding pore size distribution curve of S-N-MC.

to the clear interface between S-MC and S-N, the special lattice structure has abundant active sites for adsorbing/transforming the electrons. The clear shell and internal multi-void structure also guarantee the structural stability and enough lithium storage for achieving good electrochemical performance.[27] Through the SAED of the S-N, S-MC and S-N-MC, the physical phases of the three samples were further confirmed.

Rietveld refinement plots of the XRD patterns of the S-MC and S-N-MC (in Fig. 3g and h) confirmed the co-presence of the two cubic phases. Table S3† lists the refinement results; the unit cell volume of S-N-MC (568.548 Å^3) is much larger than that of S-MC (554.142 Å^3), attributed to the ion-size effect. Mn^{2+}/Co^{2+} in the lattices are partially replaced by Ni^{2+} ions with much larger size, leading to the increases in the unit cell volume. The specific lattice parameters of S-N, S-MC and S-N-MC two parts were calculated as 4.17, 8.21 and 8.24 Å, respectively, indicating that the special structure of S-N-MC offers the advantageous transport path for ions/electrons and the mixture of the M^{2+} ions (M = Ni, Mn and Co). Normally, the changes in the crystal structure stem from the partial substitution of atoms, along with the lack of oxygen to some degree. As described above, the improvement of electron/ion transport, Li^+ ion diffusion and electrochemical capacity all benefit from better electrical conductivity and active sites for the redox reactions supplied by the oxygen vacancies.[28,29]

Nickel element is important in forming optimal structures that have the best energy storage effect. Hence, various S-N1-MC and S-N2-MC samples were prepared with increased and decreased ratios of nickel. The surface morphologies with different ratios of nickel are similar to the S-N-MC, based on the SEM (in Fig. S1b and c†), but the thickness of the edge layer nickel oxide phase is different (in Fig. 3j and k), which is in agreement with the XRD results (in Fig. 3l). S-N-MC presented the strongest diffraction peak among the three samples, which influenced the electrochemical performance (see Fig. 6f). Besides, the corresponding ICP-OES results for the combined electrode are listed in Table S2.† The N_2 adsorption/desorption tests of the S-N-MC, S-MC and S-N (Fig. 3i and Fig. S2a, b†) all demonstrate the mesoporous structure and their corresponding pore sizes are 16, 33 and 6 nm. S-N-MC presented a smaller surface area (29.4 $m^2\ g^{-1}$) than S-MC (63.3 $m^2\ g^{-1}$) and S-N (62.3 $m^2\ g^{-1}$), as seen in Table S4.† The above results of the phase analysis of the three samples are all connected to the above structural characteristics.

The XPS analysis of S-N-M was also implemented to investigate the changes in the valence states and bond energies among the ions. The survey spectrum (in Fig. S3a†) confirmed that all the metallic elements (Ni, Co, Mn) and O were normalized by contact with the C 1s peak (285.9 eV). The Mn 2p spectrum was fitted and divided into six peaks (in Fig. 4a). Two

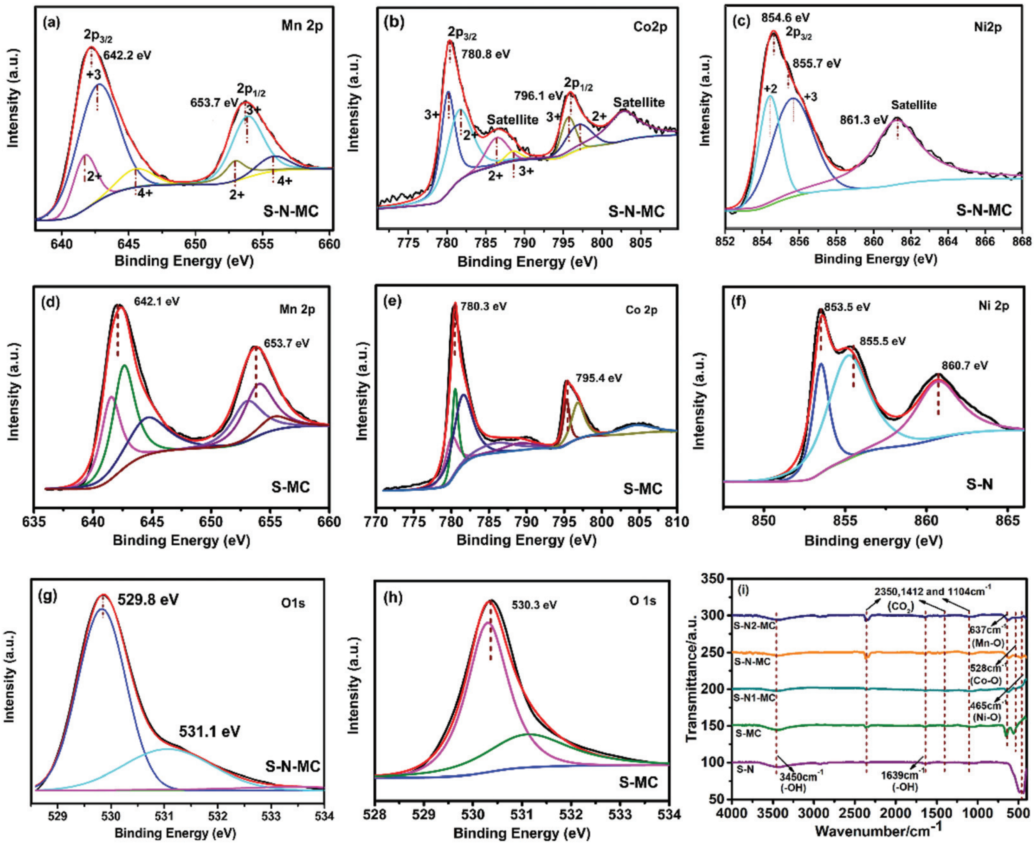

Fig. 4 Rietveld refinement plots of the XPS patterns of S-N-MC, S-MC and S-N for Mn 2p (a and d), Co 2p (b and e) and Ni 2p (c and f); O 1s (g and h) of S-N-MC and S-MC; (i) FT-IR of the prepared samples.

main peaks at 642.2 eV and 653.7 eV represent $2p_{3/2}$ and $2p_{1/2}$ with a separation of 11.5 eV, respectively. The Mn 3s spectrum (Fig. S3b†) presented two peaks attributed to the multiplet splitting of the 3s core-hole state. The extent of peak splitting is usually an important indicator of valence. The idealized splitting of the 3s orbital was about 5.5 for Mn (III);[29] therefore, the peak separation of 5.1 eV confirmed that Mn^{3+} was abundant in the sample. In the Co 2p spectrum (in Fig. 4b), Co $2p_{3/2}$ and Co $2p_{1/2}$ peaks appeared at 780.8 and 796.1 eV, which explicitly verified the main presence of Co(II) and Co(III). The Co 2p spectrum was divided into five peaks based on the spectrum of Co_3O_4. For the two spin–orbit doublets with the binding energies of 780.1 eV ($2p_{3/2}$) and 781.84 eV ($2p_{3/2}$), the $2p_{3/2}$–$2p_{1/2}$ splitting was around 15.45 eV, corresponding to Co^{3+}.[30,31] The fitting results of the Ni 2p are shown in Fig. 4c. Two peaks at 855.7 eV and 854.6 eV correspond to the existence of Ni^{3+} and Ni^{2+}, respectively.[32] A peak at 861.3 eV was indicative of Ni (II/III) satellites and was fitted.[31,33] The Mn 2p, Co 2p and Ni 2p spectra suggest the co-existence of Ni(II/III), Mn(II/III) and Co(II/III) in S-N-MC. The O 1s spectrum (in Fig. 4g) showed two contributions at 529.8 and 531.1 eV, which were assigned to the oxygen in metal–oxygen bonds (Ni–O, Mn–O and Co–O) and the oxygen existing in surface-adsorbed water or hydroxyl, respectively.[34,35]

Remarkably, the binding energies of the pure metallic Mn (638.8 eV), Co (778.2 eV) and Ni (852.8 eV) are smaller as compared to Mn 2p (642.2 eV), Co 2p (780.8 eV) and Ni 2p (854.4 eV), respectively, in the composite S-N-M.[36] Conversely, the binding energy of elemental O (530.2 eV) is higher than the O 1s binding energy (529.8 eV, Fig. 4g).[37] The abnormal bond energies confirmed the electron transfer process from the metal elements to O in S-N-MC. The binding energy of Mn 2p and Co 2p increased by 0.1 eV and 0.5 eV, respectively, as compared to the pure S-MC (642.1 eV and 780.3 eV, Fig. 4d and e). The binding energy of Ni 2p for S-N-MC is 1.1 eV higher than that of pure S-N (853.5 eV, see Fig. 4f) and the binding energy of O 1s is a litter smaller than that of the pure samples (in Fig. 4g, h and Fig. S4b†). The above results regarding the transformation of the atomic binding energy of S-N-M illustrate the electronic interactions in the interface region hybrid component, which contribute to the optimization of the electronic environment around the metal atom in the hybrid region of each component.[38]

FT-IR analysis was carried out (Fig. 4i) to detect the composition of the above-mentioned samples. The apparent absorption band in the high-frequency region at about 3450 cm^{-1} is due to the vibration of the –OH in free water droplets or physically adsorbed water molecules.[38] The absorption bands between 2500 and 2000 cm^{-1} were due to the samples absorbing carbon dioxide from the air. The absorption bands at 671, 568 and 464 cm^{-1} represent the stretching vibration of the Mn–O tetrahedron, Co–O octahedron and Ni–O tetrahedron, further revealing the formation of S-N-MC nanostructures; hence, the samples exhibited high electrochemical activity and few defects.[39]

3.2 Electrochemical Li-ion storage performance

Based on the above phase analysis, the structure–activity relationship was further studied. CV measurements were carried out (parameter setting: 0.1 mV s^{-1}) and the initial scan curve was somewhat different from the subsequent cycles, particularly in the charging branch, as shown in Fig. 5a. Two reduction peaks were seen in the initial redox cycling, located at about 1.21 and 1.09 V, respectively, which may be due to the S-N-MC being resolved into Ni, Mn, Co, Li_2O, the partial decomposition of the organic electrolyte and the formed SEI film.[40,41] Another relatively broad oxidation peak at around 1.45 V can be attributed to the alloying process of Ni–Li, Mn–Li and Co–Li,[42] while the oxidation peak at 1.95 V could be due to the extra oxidation reactions of Mn(II), Co(II) and Ni(II). The four strong peaks in the primary scan shifted slightly into the strong peaks at 1.06 V and 2.05 V in subsequent curves. These remained steady in subsequent cycles because a partially stable SEI film was formed from kinetic activation on the electrode surface.[40,43] Therefore, the main problem was the appearance of the SEI film after the primary scan, which determined the difference in the subsequent CV curves as compared to the first one. The superposition of the CV curves indicated the excellent reversibility of the electrode. The CV testing of the S-MC and S-N electrodes (see in Fig. S5a and b†) also exhibited strong and sharp peaks, which were attributed to the reversible reduction/oxidation process of Mn ↔ $Mn^{4+}/Mn^{3+}/Mn^{2+}$, Co ↔ Co^{3+}/Co^{2+}, Ni ↔ Ni^{3+}/Ni^{2+}, the alloying/dealloying reactions of Li–metal alloys and the occurence of some organic side reactions.[44,45] For the above analysis, Li^+ insertion/extraction reactions corresponding to the electrode were believed to proceed as follows:

$$NiO + 2Li^+ + 2e^- \leftrightarrow Ni + Li_2O \tag{1}$$

$$MnCo_2O_4 + 8Li^+ + 8e^- \rightarrow Mn + 2Co + 4Li_2O \tag{2}$$

$$Mn + 2Co + 3Li_2O \leftrightarrow MnO + 2CoO + 6Li^+ + 6e^- \tag{3}$$

According to the galvanostatic discharge/charge (GDC) tests, Fig. 5b reveals the 1st, 2nd, 10th, 100th and 500th cycles of the S-N-MC electrode at the current density of 500 mA g^{-1}. In the primary cycle, the S-N-MC electrode delivered a high discharge capacity (1487.7 mA h g^{-1}) and charge capacity (955 mA h g^{-1}) with irreversible loss of about 35.8%, still beyond the theoretical capacity of NiO (718 mA h g^{-1}) and $MnCo_2O_4$ (900 mA h g^{-1}). The irreversible capacity loss that occurred in the primary scan could be explained by the decomposition of the organic electrolyte and the formed SEI film; the additional initial electrochemical capacity was due to the oxidation decomposition in the high potential region of the partial SEI film.[32,46] The discharge plateaus (marked as black rectangles) at 0.52 V–1.0 V and that of the charge at 1.3 V–1.5 V/1.7 V–2.3 V correspond to the lithium alloying and dealloying processes.[44] Furthermore, starting with the second lap, the discharge/charge potential plateau presented some slight skewing, which was in agreement with the CV curve analysis (Fig. 5a).[28,42,43] The discharge/charge capacity of the S-N-CM

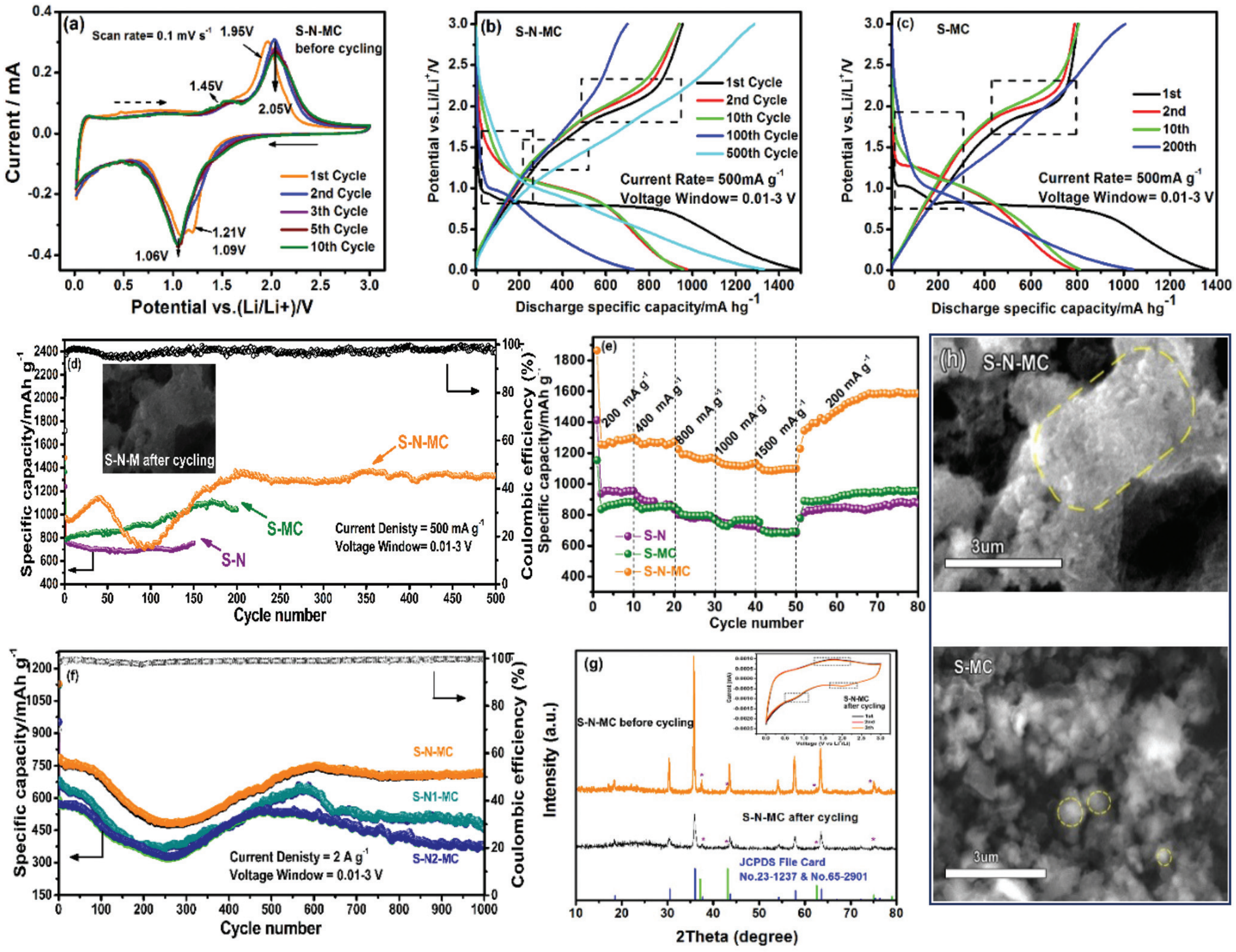

Fig. 5 Electrochemical performance between 0.01–3.0 V: (a) the CV curves of the S-N-MC electrode at a scan rate of 0.1 mV s^{-1}. (b and c) The discharge/charge curves of S-MC and S-N-MC at 500 mA g^{-1}; (d) the discharge cycling performances of S-N, S-MC and S-N-MC at 500 mA g^{-1}; (e) the rate performances of S-N, S-MC and S-N-MC; (f) the discharge cycling performances of S-N-MC, S-N1-MC and S-N2-MC at 2 A g^{-1}. (g) XRD patterns and CV spectra of the S-N-MC electrode after 500 cycles at 500 mA h g^{-1}. (h) SEM images of S-N-MC, S-MC after cycling at 500 mA g^{-1}.

was about 976/936 mA h g^{-1}, resulting in the coulombic efficiency increasing to 96% and remaining in the following cycles. On comparison of the S-MC (Fig. 5c) and S-N (Fig. S5c†), the loss ratio of the discharge/charge capacity (corresponding to the discharge/charge capacity of 1360/801 mA h g^{-1} and 1240/790 mA h g^{-1}) in the first lap were 41% and 37%, respectively. The above-mentioned CV results and GDC tests together explain the electrochemical mechanism.

Fig. 5d compares the cycling properties of S-N-MC, S-MC and S-N at 500 mA g^{-1}. The batteries with S-N-MC anodes exhibited the best specific electrochemical performance among the three electrodes. The discharge capacities at 500 mA g^{-1} of S-MC (1040 mA h g^{-1} after 200 cycles) and S-N (760 mA h g^{-1} after 150 cycles) lagged far behind that of S-N-MC (1330 mA h g^{-1} after 500 cycles). The discharge capacities of the S-N-MC electrode maintained a slight uptick in the initial 40 cycles. This phenomenon indicates a process of slow activation because the active material cannot fully come in contact with the electrolyte at the beginning of the measurement. Moreover, a stable SEI layer is built after the initial cycles, which is also reflected in the slight capacity increase.[44,47] The discharge curve is similar to the V-type, which can be understood from two aspects. (i) The decrease in capacity is due to the poor conductivity of TMOs with reinforced polarization. (ii) The subsequent recovery of capacity is mainly attributed to decreased polarization, resulting from a stable physical structure and exposed abundant active sites at the heterogeneous interface during the repeated cyclic process, thus leading to the increscent reversible capacity of the S-N-MC. The coulombic efficiencies of the S-N-MC anodes were excellent (above 97%) during all the cycles, thus confirming the heterogeneous S-N-MC as an excellent energy conversion system. Fig. 5e shows the rate capability of S-N-MC with discharge capacities of 1293, 1245, 1156, 1092 and 1060 mA h g^{-1} at 200, 400, 800, 1000, and 1500 mA g^{-1}. After recovering to 200 mA g^{-1}, the corresponding capacity could almost be maintained, with a later slow increase, indicating the excellent structural stability of the S-N-MC composite. The rate performances of S-MC and S-N were both inferior as compared to S-N-MC.

Fig. 5f shows the cycling at 2 A g^{-1} during 1000 cycles; the discharge specific capacity of S-N-MC was still satisfactory and the coulombic efficiency was maintained at 99% in the long cycling process. In contrast to the long-term cycling process of S-N-MC, the S-N1-MC (470 mA h g^{-1}), S-N2-MC (385 mA h g^{-1}) and other results in the literature all were far from the heterostructured S-N-MC (718.8 mA h g^{-1}), as shown in Table S6.† The higher capacities of S-N-MC could mainly be ascribed to the special heterostructure and the non-closed shell structure. The S-N-MC presented an amorphous nature after a long charge and discharge cycle test, which indicated the reduction of crystallinity of the fresh electrode, based on the XRD and CV results (in Fig. 5g). However, on comparing the graphs before and after the cycling, all the diffraction peaks were basically in the same position, which indicated the excellent stability of S-N-MC in the deep cycling process. The morphology of the S-N-MC was retained, based on the SEM image (in Fig. 5h, in contrast to that of S-MC), resulting in excellent electrochemical performance.

Through the characterization of the electrochemical cycle of S-N-MC, the reversible capacity presented a tendency toward going from instability to stability. The characteristic properties of transition metal oxides and the structural degradation of the electrode caused the irreversible decay of the capacity during the initial cycles. The increased electrode resistance and irreversible loss of lithium-ions in the resulting SEI film caused the initial capacity decay.[28,48] However, the discharge capacity reached a stable state after fluctuating, which was attributed to the heterostructure and nonclosed core–shell structure. The uniform non-closed shell structure with inner voids can provide four advantages: enough space for storing Li^+, adequate infiltration of the electrolyte, enhanced ion diffusion and buffering of the volume change during cycling.[49] Additionally, based on the electric field effect in the heterogeneous interface, the increased surface dynamics facilitate charge transport, and reducing the concentration polarization prevent an efficient redox action from the shock of the ultrahigh current density.

3.3 Li reaction kinetics

Given the reaction kinetics of the electrodes, the CV measurements at 0.2–1.0 mV s^{-1} are shown in Fig. 6a. The relationship

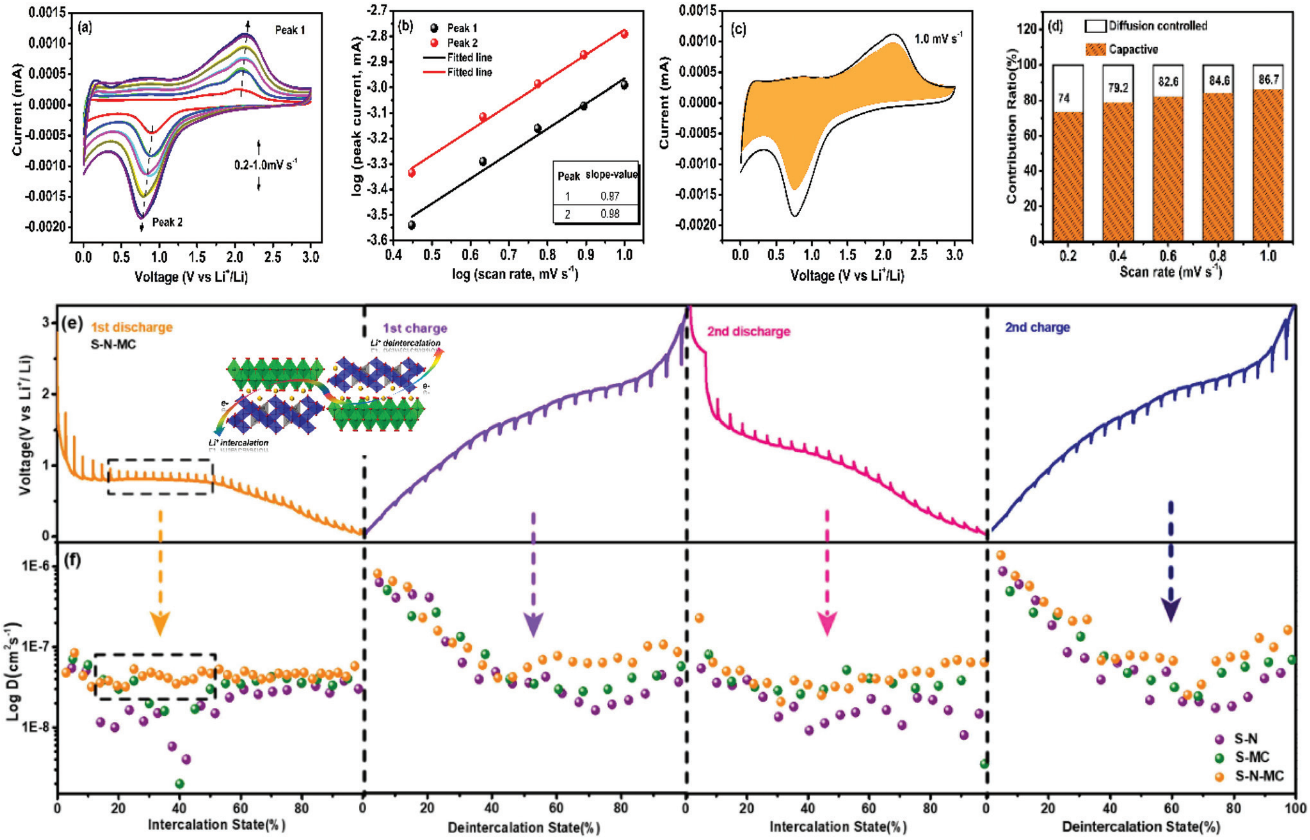

Fig. 6 Electrochemical kinetics analysis: (a) CV curves at different scan rates from 0.2 to 1.0 mV s^{-1}, (b) corresponding log(i) *versus* log(v) plots at specific peak currents. (c) CV curve with the pseudocapacitive fraction shown by the shaded area at a scan rate of 1.0 mV s^{-1}. (d) Bar chart showing the percent of pseudocapacitive contribution at different scan rates. (e and f) GITT curves and the corresponding Li^+ diffusion coefficient at different discharge/charge state of the S-N-MC electrode.

between the current (i) and scanning rate (v) can be expressed as follows: $i = av^b$,[50,51] where a and b are constants and b is the range from 0.5 to 1.0. For $b = 0.5$, the electrochemical reaction is a diffusion-controlled process, whereas $b = 1.0$ represents a capacitive-controlled process. The log(i) *vs.* log(v) plot will be used to analyze the b value, as shown in Fig. 6b. The values of the two redox peaks were 0.97 and 0.98, indicating that the redox reactions of the S-N-MC electrode favored the capacitive process, causing the excellent enhanced reversible capacity and cycling stability. The b values of S-MC and S-N are also summarized in Fig. S6.† The pseudocapacitive contribution can be estimated by the equation i (V) = $k_1v + k_2v^{1/2}$. The capacitive-controlled and diffusion-controlled contributions are represented by k_1v and $k_2v^{1/2}$, respectively. The capacitive-controlled contribution illustrated by the orange shadow was 86.7% for S-N-MC at 1.0 mV s^{-1} (in Fig. 6c). The contribution of S-N-MC is more prominent than that of S-MC and S-N (in Fig. S6†) because of the abundant two-phase surfaces from the coexistence of the two phases with small crystalline domains and rich active sites. With the increase of the scanning speed, the contribution rate of pseudocapacitance gradually increased from 74% to 86.7%, as shown in Fig. 6d. In any case, the pseudocapacitance supports the charge storage of S-N-MC with the fast kinetics features of the electrochemistry, resulting from the generation of lattice defects and the adjustment of the electronic environments with changes in the interatomic binding energies in the interface region.

Based on the above reaction mechanism (eqn (1)–(3)), if the material unevenness and polarization effect are ignored, the above conversion reactions of the metallic oxide (MO) correspond to the voltage platform and the electromotive force (emf) of about 1.04–1.95 V and 0.75 V (*vs.* Li/Li$^+$), respectively, judging by the Nernst equation:[33,52] $\Delta G = \Delta G_f^\circ(\mathrm{Li_2O}) - \Delta G_f^\circ(\mathrm{MO}) = -nEF$. Due to the alloying conversion reaction that occurs below the range of the emf value (*vs.* Li/Li$^+$), q, the reverse conversion reaction needs to practically be beyond the emf. From the polarization, the average charge/discharge plateaus at about 2.15 V and 0.75 V correspond to the oxidation and reduction of MO, respectively (Fig. 6e). Hence, the GITT curves present the alloying and dealloying processes with effective polarization for the active material. GITT was performed to expound on the electrochemical process of S-N-MC regarding ion diffusion. The minimum of the diffusion coefficient in the circulation process appears on the voltage plateau of each redox platform (Fig. 6f and Fig. S7†), where the Li$^+$ completes the deep embedding/ejecting process. On the whole, the Li$^+$ diffusion coefficient of S-N-MC presents relatively smaller fluctuations, higher than that in S-N and S-MC, suggesting that conductivity and ion diffusion increase together in the ternary metallic compounds. On the one hand, the phase interface restricts the normal growth of the crystal plane, which leads to the production of active sites and defect sites with fast ion diffusion. On the other hand, the different voltage platform and asynchronous reactions of a mixture of MO would relieve the pressure of ion transport, which is beneficial to the diffusion of Li$^+$.

Fig. 7a shows the EIS spectra of the electrodes at different current densities before and after the deep cycles between 0.01 and 3 V. For the fresh cells of the electrode material, the R_{ct} values of S-N-MC, S-MC and S-N were 50.3, 127.9 and 134.2 Ω, respectively. Therefore, the prepared S-N-MC possessed the best electronic conductivity profiting from the special non-closed core–shell heterostructure. After 500 cycles at 500 mA g^{-1}, the R_{ct} of S-N-MC, S-MC, and S-N increased to 82.1, 233.2 and 332.8 Ω. The EIS spectra of S-N-MC, S-N1-MC, and S-N2-MC are also shown in Fig. 7b, and the R_{ct} values before and after cycling at 1000 mA g^{-1} further confirmed the strength of a reasonable combination of the different phases. By comparing the R_{ct} increases, that of S-N-MC appeared to be the lowest after the cycling process (see Table S5† for details). This can be interpreted as the special heterostructure of S-N-MC providing a suitable transmission route for the ions and electrons, resulting in lower resistance to electrochemical reactions.

To investigate the charge distributions on the heterostructure, the first-principles density functional theory (DFT) calculations were carried out. In good agreement with the above XPS analysis, the strong electronic interactions on the interface led to the transfer and recombination processes of

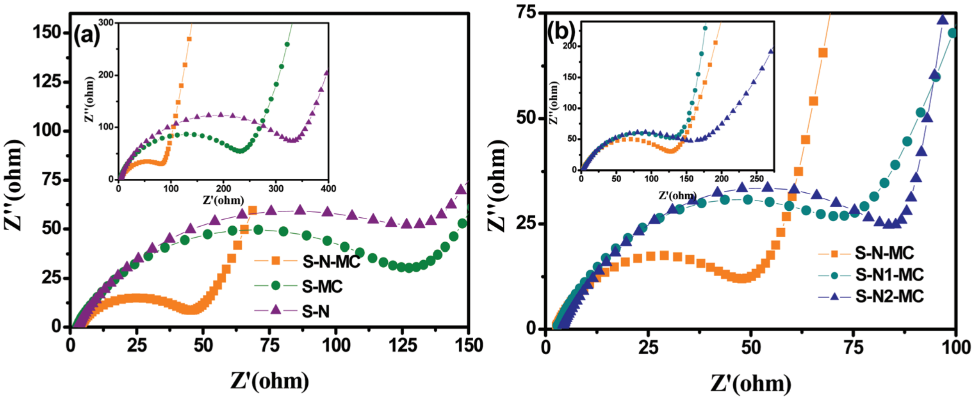

Fig. 7 EIS spectra of the prepared electrodes after cycles at 500 mA g^{-1} (a) and 2 A g^{-1} (b) between 0.01 and 3 V; the insets show the EIS spectra of the fresh electrodes before cycling.

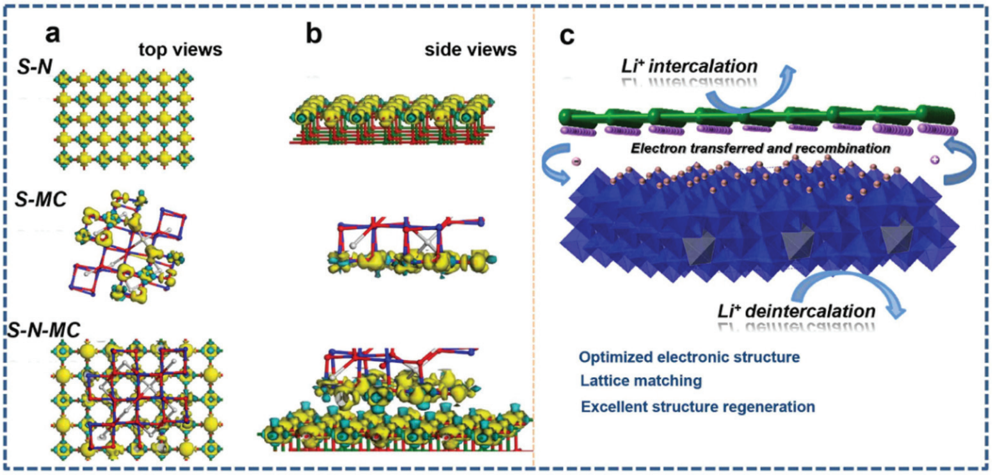

Fig. 8 (a and b) DFT calculation studies of the S-N, S-MC and S-N-MC interfaces: the top and side views of the electron density difference maps for the S-N, S-MC and S-N-MC interfaces. Yellow and cyan isosurfaces represent charge accumulation and depletion. Green, blue, gray, and red balls represent Ni, Co, Mn, and O atoms, respectively. (c) The corresponding properties and illustration of the ion/electron transport mechanism process.

interface atoms (Mn, Co, Ni and O). Through the electron density difference maps for S-N, S-MC and S-N-MC in the top view and side view (Fig. 8a and b), it was observed that the electrons were redistributed after assembling single components (S-N and S-MC), especially around those defective bits in the S-N-MC. These phenomena clearly illustrate that the hybrid interface not only provides abundant active sites for electron transfer but also provides an integrative path for the charge diffusion, thus enhancing the reaction kinetics. As illustrated in Fig. 8c, electron transfer and accumulation among the Ni–Co–Mn–O at the defect sites in the interface boost the optimized electronic structure after the lattice matching at the primal cycle and finally result in the structure regeneration. The hybrid of S-N and S-MC resulted in an anomaly in the electronic structure, leading to transformation and subsequent redistribution. The electrons that accumulated locally around the defect sites promoted the redox reaction for the enhanced active sites, whereas the transfer of electrons caused vacancy accumulation, which favored the reaction kinetics.[53] Therefore, the optimized charge diffusion path and electronic structure from the electronic transfer and recombination on the hybrid interface contributed to the stable structure regeneration and outstanding energy storage of the hybrid electrode material for LIBs.

4. Conclusions

In summary, a uniform non-closed core–shell NiO-$MnCo_2O_4$ heterostructured ternary metal oxide has been synthesized through the calcination of an oxalate precursor. Satisfactorily, it displayed a high initial capacity of 1129 mA h g^{-1} at 2 A g^{-1} with high coulombic efficiency of 99% after 1000 cycles, advanced capacity retention of 718.8 mA h g^{-1} at 2 A g^{-1}, and persistent cycles after impact at different ionization densities. The S-N-MC electrode appeared to be characteristic of pseudocapacitance and a higher diffusion coefficient, resulting in high rate capability and fast electrochemical kinetics. The experimental results suggest that a suitable nickel content is beneficial to the two-phase heterogeneous structure; too much will produce a thick core–shell without adequate infiltration of electrolyte and too little is not appropriate for the formation of a stable heterogeneous structure. Moreover, the void space inside the structure is conducive to electrolyte penetration and accommodates the volume expansion during the ion/electron transport, resulting in the concentration polarization of the electrode being weakened to some degree. The compact nonclosed outer shell boosts the diffusivity and maintains a stable structure, thereby manifesting as the stability of the electrochemical properties. The heterostructure with the optimized electronic environment in the two-phase interface that exists simultaneously at the boundary contributes abundant lattice defect sites with the rearrangement of electrons and active sites, which expands the transport path and capacitive storage for electrons/ions and effectively improves the electrochemical performance. It is believed that our present work will provide effective ideas for fabricating various hybrid electrode materials with excellent electrochemical properties for energy storage applications of LIBs.

Conflicts of interest

The authors declare no conflict of interest.

Acknowledgements

This work was supported by the National Natural Science Foundation of China (Grant No. 21276286 and 21271187), the Open-End Fund for Valuable and Precision Instruments of Central South University (CSUZC201622), Natural Science

Foundation of Hunan Province China (Grant No. 2019JJ50205), Scientific Research Foundation of Hunan Provincial Education Department, China (Grant No. 18B347).

References

1 D. Larcher and J. M. Tarascon, *Nat. Chem.*, 2015, **7**, 19–29.
2 Z. Fan, J. Liang, W. Yu, S. Ding, S. Cheng, G. Yang, Y. Wang, Y. Xi, K. Xi and R. V. Kumar, *Nano Energy*, 2015, **16**, 152–162.
3 C. S. Yan, G. Gang, X. Zhou, J. X. Sun and C. D. Lv, *Adv. Funct. Mater.*, 2016, **26**, 1428–1436.
4 C. Kim, J. W. Jung, K. R. Yoon, D. Y. Youn, S. Park and I. D. Kim, *ACS Nano*, 2016, **10**, 11317–11326.
5 B. Dunn, H. Kamath and J. M. Tarascon, *Science*, 2011, **334**, 928–935.
6 Y. Zhong, M. Yang, X. Zhou, Y. Luo, J. Wei and Z. Zhou, *Adv. Mater.*, 2015, **27**, 806–812.
7 H. Wu, G. Yu, L. Pan, N. Liu, M. T. McDowell and Z. Bao, *Nat. Commun.*, 2013, **4**, 1943.
8 A. L. M. Reddy, S. R. Gowda, M. M. Shaijumon and P. M. Ajayan, *Adv. Mater.*, 2012, **24**, 5045–5064.
9 L. Shen, X. Zhang, E. Uchaker, C. Yuan and G. Cao, *Adv. Energy Mater.*, 2012, **2**, 691–698.
10 A. Debart, L. Dupont, P. Poizot and J. B. Leriche, *J. Electrochem. Soc.*, 2001, **148**, A1266.
11 P. Poizot, S. Laruelle and S. Grugeon, *Nature*, 2000, **407**, 496–499.
12 J. Jiang, Y. Li, J. Liu, X. Huang, C. Yuan and X. W. D. Lou, *Adv. Mater.*, 2012, **24**, 5166–5180.
13 H. Liu, Z. Mai, X. Xu and Y. Wang, *Dalton Trans.*, 2020, **49**, 2880–2887.
14 A. F. Shaikh, R. S. Kalubarme and M. S. Tamboli, *ChemistrySelect*, 2017, **2**, 4630–4637.
15 F. Yang, W. Li and B. Tang, *Chem. – Eur. J.*, 2018, **334**, 2021–2029.
16 Y. Zhang, Q. Zhuo, X. Lv, Y. Ma, J. Zhong and X. Sun, *Electrochim. Acta*, 2015, **178**, 590–596.
17 Y. F. Wang and L. J. Zhang, *J. Power Sources*, 2012, **209**, 20–29.
18 Q. Q. Xiong, X. H. Xia, J. P. Tu, J. Chen and Y. Q. Zhang, *J. Power Sources*, 2013, **240**, 344–350.
19 H. Long, T. Shi and S. Jiang, *J. Mater. Chem. A*, 2014, **2**, 3741–3748.
20 Y. Lin, K. Sun, S. Liu, X. Chen, Y. Cheng and J. Jun, *Adv. Energy Mater.*, 2019, **9**, 1901213.
21 L. Huang, F. Peng, H. Wang, H. Yu and Z. Li, *Catal. Commun.*, 2009, **10**, 1839–1843.
22 Y. Zheng, T. Zhou, C. Zhang, J. Mao, H. K. Liu and Z. Guo, *Angew. Chem.*, 2016, **128**, 3469–3474.
23 W. Zhou, C. Cheng, J. Liu, Y. Y. Tay, J. Jiang and X. Jia, *Adv. Funct. Mater.*, 2011, **21**, 2439–2445.
24 L. Yu, G. Zhang, C. Yuan and X. W. D. Lou, *Chem. Commun.*, 2013, **49**, 137–139.
25 J. Li, S. Xiong, Y. Liu, Z. Ju and Y. Qian, *ACS Appl. Mater. Interfaces*, 2013, **5**, 981–988.
26 S. Xiong, J. S. Chen, X. W. Lou and H. C. Zeng, *Adv. Funct. Mater.*, 2012, **22**, 861–871.
27 L. Hu, C. Dai, H. Liu, Y. Li, B. Shen and Y. Chen, *Adv. Energy Mater.*, 2018, **8**, 1800709.
28 Q. Li, G. Zhu, Y. Zhao, K. Pei and R. Che, *Small*, 2019, **15**, 1900069.
29 C. Hou, Y. Hou, Y. Fan, Y. Zhai, Y. Wang and Z. Sun, *J. Mater. Chem. A*, 2018, **6**, 6967–6974.
30 J. L. Gautier, E. Rios, M. Gracia, J. F. Marco and J. R. Gancedo, *Thin Solid Films*, 1997, **311**, 51–57.
31 Y. Zhai, H. Mao, P. Liu, X. Ren, L. Xu and Y. Qian, *J. Mater. Chem. A*, 2015, **3**, 16142–16149.
32 T. Li, X. H. Li, Z. X. Wang, H. J. Guo, Q. Y. Hu and W. J. Peng, *Electrochim. Acta*, 2016, **191**, 392–400.
33 Y. J. Mai, S. J. Shi, D. Zhang, Y. Lu, C. D. Gu and J. P. Tu, *J. Power Sources*, 2012, **204**, 155–161.
34 S. L. Xiong, J. S. Chen, X. W. Lou and H. C. Zeng, *Adv. Funct. Mater.*, 2012, **22**, 861–871.
35 T. He, X. Wang, H. Wu, H. Xue, P. Xue and J. Ma, *ACS Appl. Mater. Interfaces*, 2017, **9**, 22490–22501.
36 K. Wang, X. She and S. Chen, *J. Mater. Chem. A*, 2018, **6**, 5560–5565.
37 L. Zhou, M. Shao, C. Zhang, J. Zhao, S. He, D. Rao, M. Wei, D. G. Evans and X. Duan, *Adv. Mater.*, 2017, **29**, 1604080.
38 F. L. Bei, X. L. Hou and D. Li, *Chem. – Eur. J.*, 2011, **17**, 5958–5964.
39 S. Panigrahi, S. Basu and T. Pal, *J. Phys. Chem. C*, 2007, **111**, 4596–4605.
40 G. Huang, S. Xu, S. Lu, L. Li and H. Sun, *ACS Appl. Mater. Interfaces*, 2014, **10**, 7236–7243.
41 L. Yu, L. Zhang, H. B. Wu, G. Zhang and D. X. W. Lou, *Energy Environ. Sci.*, 2013, **6**, 2664–2671.
42 J. Li, S. Xiong, X. Li and Y. Qian, *Nanoscale*, 2013, **5**, 2045–2054.
43 R. Zhang, D. Shen, M. Xu, D. Feng, W. Li, G. Zheng and R. Che, *Adv. Energy Mater.*, 2014, **4**, 1–7.
44 G. Huang, S. Xu, Z. Xu, H. Sun and L. Li, *ACS Appl. Mater. Interfaces*, 2014, **6**, 21325–21334.
45 M. Wang, X. Yu and L. Hou, *Chem. Eng. J.*, 2018, **351**, 930–938.
46 C. Fu, G. Li, D. Luo, X. Huang, J. Zheng and L. Li, *ACS Appl. Mater. Interfaces*, 2014, **6**, 2439–2449.
47 W. Yang, Z. Gao, J. Ma, X. Zhang, J. Wang and J. Liu, *J. Mater. Chem. A*, 2014, **2**, 1448–1457.
48 M. V. Reddy, Y. Xu and V. Rajarajan, *ACS Sustainable Chem. Eng.*, 2015, **3**, 3035–3042.
49 X. Li, L. Zhou, Y. Wei, F. Zhang and D. Zhao, *J. Am. Chem. Soc.*, 2015, **137**, 5903–5906.
50 L. Shen, H. Lv, S. Chen, P. Kopold, P. A. Vanaken and X. Wu, *Adv. Mater.*, 2017, **29**, 1533–1541.
51 S. Lou, X. Cheng, Y. Zhao, A. Lushington, J. Gao and Q. Li, *Nano Energy*, 2017, **34**, 15–25.
52 H. Li, P. Balaya and J. Maier, *J. Electrochem. Soc.*, 2004, **151**, A1878–A1885.
53 Y. Jia, L. Zhang, G. Gao, H. Chen and B. Wang, *Adv. Mater.*, 2017, **29**, 1700017.